ACS APPLIED NANO MATERIALS

www.acsanm.org Letter

Preserved Magnetic Functionality in Freestanding Strain-Engineered Nanocomposite Thin Films

Carlos Alfonso Rodríguez Cortéz, Moussa Mebarki, Bruno Berini, Dominique Demaille, Vincent Polewczyk, Yunlin Jacques Zheng, Pal Bhuyan, Boris Vodungbo, Emmanuelle Jal, Horia Popescu, Nicolas Jaouen, Yves Dumont, Marcel Hennes, and Franck Vidal*

Cite This: *ACS Appl. Nano Mater.* 2026, 9, 9206–9212 Read Online

ACCESS | Metrics & More | Article Recommendations | Supporting Information

ABSTRACT: The development of freestanding oxide thin films enables the design of unconventional heterostructures with enhanced functionalities. Here, we explore the fabrication of membranes consisting of dense arrays of ultrathin Co_xNi_{1-x} nanowires embedded in a dielectric matrix. We present a lift-off process to create and transfer these membranes while preserving the structural and chemical integrity of the nanopillars. The large axial deformation of the metallic nanostructures is maintained, and their magnetic properties remain largely unaltered after substrate removal. This robustness enables the integration of such strain-engineered, vertically aligned nanocomposites into flexible spintronic and magnetic memory platforms.

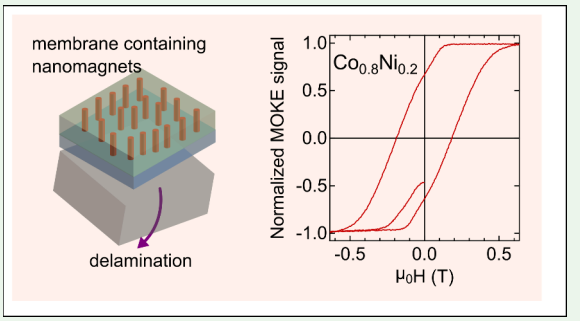

KEYWORDS: *nanocomposite, membrane, epitaxy, strain-engineering, magnetic anisotropy*

Functional oxide membranes form an emerging class of materials that has attracted increasing interest.[1,2] These single-crystal layers with a thickness ranging from a few unit cells[3] to hundreds of nm can be obtained by delamination of thin films grown by pulsed laser deposition (PLD) using soluble sacrificial layers.[4−6] After lift-off, they can be readily transferred to other substrates and can be incorporated into complex hybrid or even flexible systems.[7−10] While a broad variety of thin films have already been successfully removed from the substrates they were grown on, freestanding heterostructured layers, consisting of different phases that are epitaxially coupled to each other, have received less attention so far.[11]

In this context, self-assembled vertically aligned nanostructures (VAN) − where nm-sized columns are coherently embedded in a surrounding matrix − are particularly appealing.[12,13] A salient feature in many epitaxial VAN is their strain state governed by the lattice mismatch between the constituent phases and relaxation effects at vertical hetero-interfaces.[13,14] In these systems, the deformations imposed by the matrix on the wires can be used for precise strain-mediated control of physical properties − statically and dynamically − as has been demonstrated in earlier work.[15−17]

While the fabrication of VAN membranes appears to be an attractive route to expand the portfolio of materials available for the design of heterostructures, to the best of our knowledge, only a few reports dealing with the synthesis of freestanding composites have been published so far. This is especially true for VAN combining metallic and oxide phases. Huang et al. explored the use of $Sr_3Al_2O_6$ (SAO) sacrificial layers to obtain flexible Au-TiN VAN thin film membranes and analyzed their optical properties.[18] Tsai et al. grew Au-$BaTiO_3$ VAN[19] and successfully removed the membranes from the substrate. However, in these studies, the use of a noble metal reduced the risk of chemical modifications induced by the lift-off process. In composites that combine magnetic, metallic materials and an oxide matrix, the embedded nanowires consist of Fe, Co, Ni and their alloys[20−23] that can oxidize, potentially modifying their magnetic properties. In addition, the preservation (or loss) of vertical dilation − one of the key parameters used to control the magnetic properties in VAN − has not been analyzed in freestanding films.

In this letter, we address this issue and report on the synthesis of magnetic metal-oxide VAN membranes where the strain state of the embedded magnetic pillars is preserved. This opens perspectives for the design of heterostructures that cannot be obtained using conventional planar epitaxy methods.

In previous studies on Co_xNi_{1-x}-$SrTiO_3$ VAN, it was shown that magnetic Co_xNi_{1-x} nanopillars, with diameters below 5 nm and aligned along the growth direction, could be obtained

Received: March 5, 2026
Revised: May 5, 2026
Accepted: May 5, 2026
Published: May 8, 2026

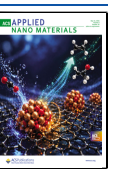

https://doi.org/10.1021/acsanm.6c00973
ACS Appl. Nano Mater. 2026, 9, 9206−9212

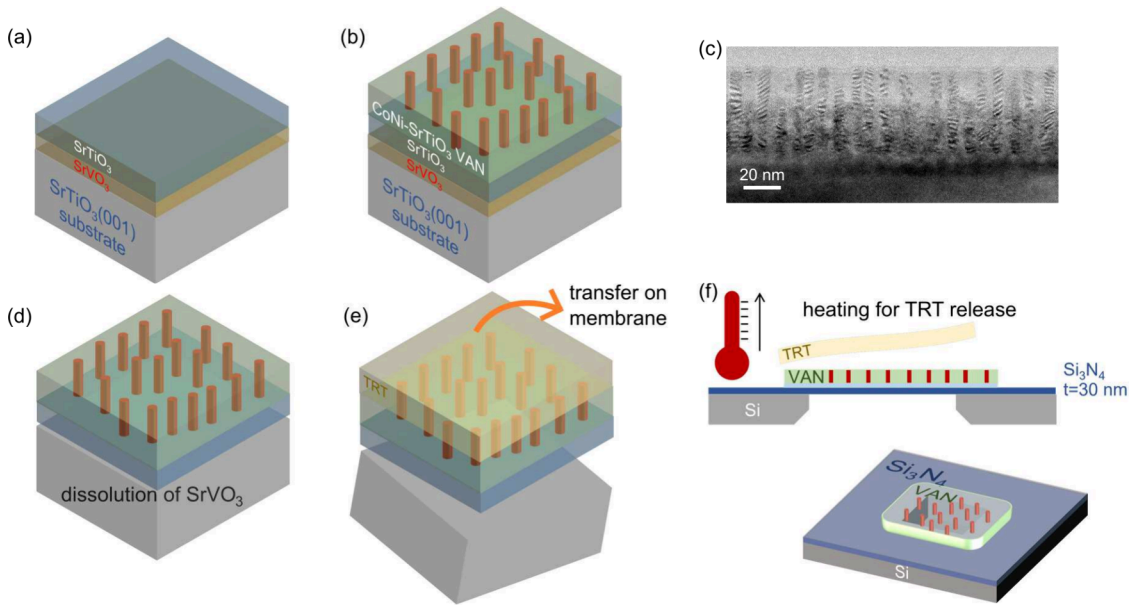

Figure 1. Growth and delamination of $Co_{0.5}Ni_{0.5}$-$SrTiO_3$ VAN membranes. (a) First growth step: pulsed laser deposition of homoepitaxial $SrVO_3$ and $SrTiO_3$ thin films on a $SrTiO_3$(001) substrate. (b) Second growth step: sequential pulsed laser deposition of a $Co_{0.5}Ni_{0.5}$-$SrTiO_3$ VAN on $SrTiO_3$/$SrVO_3$/$SrTiO_3$(001). (c) Cross-section transmission electron microscopy image of a $Co_{0.5}Ni_{0.5}$-$SrTiO_3$ VAN grown on $SrTiO_3$(001): the formation of $Co_{0.5}Ni_{0.5}$ nanopillars is evidenced by Moiré patterns. (d) Dissolution of the $SrVO_3$ sacrificial layer. (e) Removal of the substrate using a thermal release tape (TRT). (f) Transfer on Si_3N_4/Si membranes.

via pulsed laser deposition (PLD).[22] In these composites, the metallic phase grows epitaxially within the $SrTiO_3$ (STO) matrix with a cube-on-cube epitaxial relationship. Furthermore, it was demonstrated that the metallic alloy is highly strained along the out-of-plane direction, with tensile strains reaching several percent and giving rise to strong magnetoelastic effects.[22] We have thus chosen this system to explore the issue of metal-oxide VAN delamination.

The fabrication process is illustrated in Figure 1. Prior to deposition of the Co_xNi_{1-x}-$SrTiO_3$ VAN, a thin 5 nm sacrificial layer of strontium vanadate $SrVO_3$ (SVO) is deposited on the STO(001) substrate.[5] Due to the structural compatibility (aristotype $Pm\bar{3}m$ perovskite, lattice parameter 3.843 Å[24]) with the STO substrate and the low lattice mismatch, this layer grows fully strained and with a cube-on-cube epitaxy, preserving the properties necessary for the subsequent deposition of a fully epitaxial VAN. On top of the SVO layer, a thin ∼ 10 nm cube-on-cube epitaxial and fully strained STO capping layer is grown which efficiently protects the sacrificial film, and allows us to perform a transfer under ambient conditions into a second PLD chamber, where the nanocomposite thin film was eventually deposited.

The latter was grown using a sequential scheme[20] employing $SrTiO_3$, CoO and NiO targets as described in detail previously.[22] This leads to the self-assembly of nanopillars embedded in STO and aligned along the growth direction, as shown in the transmission electron microscopy images in Figure 1c, see Supporting Information for a more detailed description of growth process and transmission electron microscopy results. After PLD growth, delamination and transfer onto Si_3N_4 (SN) grid are achieved following the steps described in Figure 1 (see SI for details). In this work, three different types of freestanding VAN membranes with distinct compositions of the magnetic nanopillars were grown and analyzed in detail: $Co_{0.2}Ni_{0.8}$, $Co_{0.5}Ni_{0.5}$ and $Co_{0.8}Ni_{0.2}$. For these compositions, the embedded Co_xNi_{1-x} alloy remains in a cubic structure and the magnetostriction coefficient is positive.[22]

Optical microscopy images of two SN membranes are shown in Figures 2a,b. In these images, the transferred VAN is clearly visible. As can be seen, due to the fragility of the freestanding film, transferring large membrane areas is technically challenging. Moreover, the film may present cracks, as seen in Figure 2a. Despite this, large micrometer-sized flakes such as

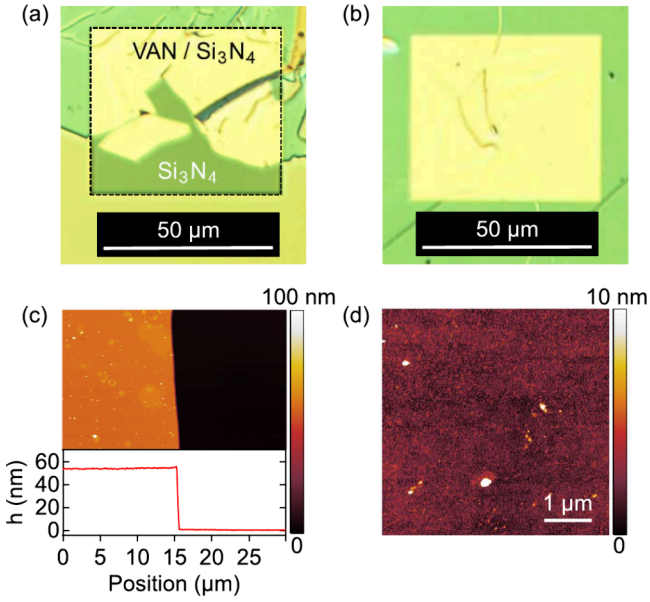

Figure 2. Delaminated membranes. (a) Optical microscopy image of a partially covered Si_3N_4 membrane window. (b) Optical microscopy image of a fully covered Si_3N_4 membrane window. (c) AFM topography scan (30 μm × 30 μm) over the edge of a flake (a profile is shown in the inset) and (d) topography scan on top of a flake (5 μm × 5 μm).

https://doi.org/10.1021/acsanm.6c00973
ACS Appl. Nano Mater. 2026, 9, 9206−9212

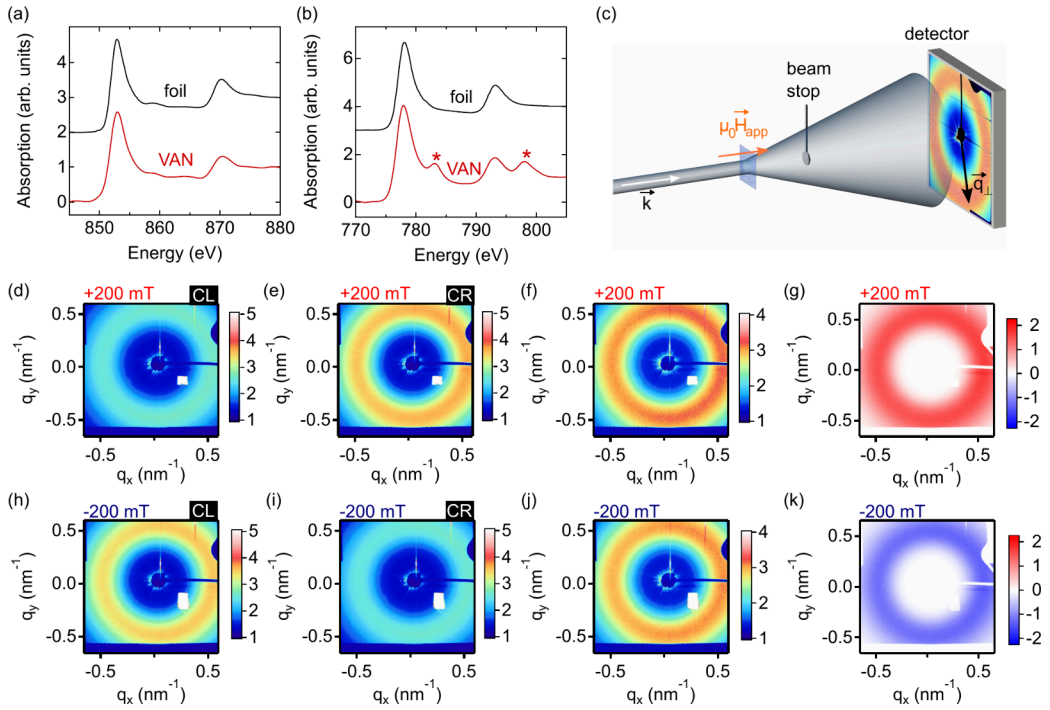

Figure 3. (a-b) X-ray absorption spectrum at the Ni (a) and Co (b) $L_{2,3}$ edges acquired in transmission for the reference metallic foils (black) and for the delaminated VAN sample (red). Red asterisks in the Co absorption spectrum highlight the contribution from minute Ba impurities. (c) Experimental configuration for XRMS measurements on delaminated VAN samples. (d-g) XRMS data gathered at the Ni L_3 edge (photon energy 853 eV) with $\mu_0 H_{app}$ = +200 mT: (d) scattering pattern acquired with circular left polarization and with (e) circular right polarization, (f) charge signal I_c, (g) magnetic signal I_m. (h-k) XRMS data obtained by tuning the X-ray energy to the Ni L_3 edge with $\mu_0 H_{app}$ = −200 mT: (h) scattering pattern acquired with circular left polarization, (i) same with a circular right polarization, (j) charge signal I_c, (k) magnetic signal I_m. Scale bars in (d-k): intensity (arbitrary units).

the one shown in Figure 2b, which can cover entire (50 × 50)μm^2 SN membrane windows, were obtained for every sample (see SI for more information on the transfer yield and flake sizes). Note that the freestanding membrane thickness determined from atomic force microscopy (AFM) measurements (Figure 2c) is found to be in excellent agreement with the nominal thickness of our deposited films (50 nm). This observation indicates the full removal of the sacrificial layer and the absence of residual material after the lift-off process. As can be seen in Figure 2d, on a local, micrometer scale, the surface of the membrane is free of cracks and voids and essentially flat, with no observable wrinkles and a RMS roughness of ≈1 nm.

Having demonstrated the possibility of transferring large flakes of delaminated VAN, the next question that arises is the preservation of the integrity of the nanoarchitecture and chemical composition of the wires upon delamination. While the structural properties of the delaminated composites can be probed using conventional X-ray diffraction (as will be demonstrated in a later part of this paper), retrieving the full chemical and magnetic information with nanometer lateral resolution is challenging, given the small diameter and large areal density of the embedded nanostructures (see the in-plane transmission electron micrograph in SI). To assess the properties of the wires after removal of the membrane from the substrate, we used a combination of X-ray absorption spectroscopy (XAS) and X-ray resonant magnetic scattering (XRMS) experiments. The experiments were performed at the SEXTANTS beamline of the SOLEIL synchrotron, on the COMET endstation, where we took advantage of the large sCMOS detector (6144 px × 6144 px, 11 μm pixel size), allowing us to access sufficiently large q-values in reciprocal space, corresponding to typical interwire distances of ≃10 nm,[25] as will be shown in the following.

Prior to measurements on VAN membranes, the beamline energy was calibrated by using the $L_{2,3}$ edge spectra of metallic Co and Ni reference foils (using a point-like photodiode detector). The corresponding XAS spectra are shown in Figures 3a,b. In a second step, the same spectra were acquired for the membranes, see Figures 3a,b. Both the Co and Ni spectra clearly exhibit a metallic character, being nearly identical to the reference foils. Within the sensitivity limits of our transmission L-edge XAS, no multiplet structure nor peak shift or broadening could be observed, which highlights the chemical integrity of the samples, i.e., the absence of oxide or hydroxide phases that might be induced in the nanowires by the dissolution process. Note that, in contrast to previous X-ray magnetic circular dichroism studies performed on CoNi VAN thin films on a substrate,[22] the spectra shown here were acquired in transmission, and not in total electron yield mode. The data are thus representative of the entire sample thickness. At the Co edge, two additional peaks are observed in the spectrum of the VAN, highlighted by red asterisks. These correspond to the X-ray absorption of Ba at the $M_{4,5}$ edges. This signal stems from minute amounts of Ba impurities in the STO matrix, which can be traced back to the PLD target used in our study.[22]

Scattering patterns were then acquired for the membranes using the sCMOS camera with X-rays tuned either to the Co or Ni L_3 edges. Data were gathered using consecutive measurements with opposite circular polarizations at a given magnetic field applied in the direction perpendicular to the plane of the membrane, along the axis of the magnetic

https://doi.org/10.1021/acsanm.6c00973
ACS Appl. Nano Mater. 2026, 9, 9206−9212

nanopillars, as illustrated in Figure 3c. The intensity patterns are denoted I_+, I_- for positive and negative helicities, respectively. From these measurements, two quantities are computed, following Rackham et al.:[26] the average $I_c = (I_+ + I_-)/2$, which, to a good approximation, corresponds to the electron-density (charge) contribution, and the (squared) magnetic ratio $I_m = R_m^2 = (I_+ - I_-)^2/(I_+ + I_-) = I_d^2/(I_+ + I_-)$, which yields information about the magnetic structure of the sample. Note that while the charge scattering intensities shown in the following correspond to I_c, the plots of the magnetic signal correspond to $\mathrm{sign}(I_d)I_m$, which allows highlighting a possible sign switching upon reversal of the magnetization.

Exemplary scattering patterns of a $Co_{50}Ni_{50}$ membrane sample at the Ni L_3 resonance peak, acquired under a magnetic field of 200 mT (sufficiently large to saturate this specific sample) are shown in Figures 3d-f (see Supporting Information for a description of the procedure used to map detector data into reciprocal space). The same measurements, performed with an applied field of − 200 mT are shown in Figures 3h-j. Note that, as expected, the obtained annular charge patterns $I_c(q)$ do not change when modifying the applied field (data not shown). From these data, information on the (in-plane) spatial distribution of embedded nano-objects can readily be extracted: the wires are randomly located and do not form any measurable pattern. They are however separated by a characteristic distance $\langle d \rangle$, which can be computed by fitting the intensity profiles $I_c(q)$ (obtained after azimuthal integration). This allows us to determine the position of the maximum q_{max}, from which $\langle d \rangle$ is calculated using $\langle d \rangle = 2\pi/q_{max}$. When analyzing the two transition metals separately (see Supporting Information for a full description of the scattering patterns obtained at the Co edge), we observe almost identical characteristic distances resulting from the charge scattering profile $I_c(q)$. On the $Co_{50}Ni_{50}$ sample for example, we get 12.52 ± 0.04 nm at the Co edge, while at the Ni edge, we calculate 12.65 ± 0.03 nm. The agreement with the periodicity value of 12.7 ± 0.6 nm obtained from the in-plane pair-correlation function measurements by transmission electron microscopy is excellent. Identical correlation lengths for Ni and Co also indicate that the two chemical species are distributed at random in the nanowires, which is in good agreement with our earlier studies.[20,22]

In order to confirm that the magnetic properties of the nanopillars are preserved upon delamination and transfer of the membranes, we performed a similar analysis using $I_m(q)$. In contrast to the charge signal, the magnetic patterns exhibit a strong field dependence (data not shown), highlighting complex field-dependent interactions between the wires, giving rise to ordering and frustration effects. However, we exclusively focus on the magnetically saturated samples here. Figures 3g and k show the magnetic intensity I_m obtained at the Ni edge for +200 mT and at − 200 mT. As mentioned earlier, $I_m(q)$ displays a sign reversal upon saturation in the opposite field direction. However, the location of the peak q_{max} is identical for both field directions and very similar at both edges: we find 12.48 ± 0.05 nm using the $I_m(q)$ profile for Co and 12.59 ± 0.04 nm for Ni, respectively. This is in excellent agreement with the previously reported results gathered from the charge scattering analysis and the TEM data. At saturation, all nanowires contribute to the magnetic scattering signal. This is additional evidence that allows us to rule out oxidation effects that would lead to "magnetically dead" wires (or parts of the wires), as this would have a measurable impact on the magnetic correlation length. Overall, the XAS and XRMS data thus point toward a full preservation of the chemical and magnetic state of the nanopillars after the delamination process.

The spectroscopic analysis described in the last paragraphs was further complemented with MOKE measurements, performed before and after releasing the membranes from the substrate. In our nanocomposite system, the magnetic anisotropy is uniaxial and dominated by shape and magnetoelastic effects, respectively: $K_u = K_{MS} + K_{me}$. The trend observed in Figures 4a-c, with increasing squareness of the hysteresis cycle and coercive field indicates an increase of the anisotropy when the cobalt content increases. Despite small changes upon removal from the substrate, this trend persists in the freestanding films. Interestingly, for the $Co_{0.2}Ni_{0.8}$-$SrTiO_3$ VAN, $\mu_0 H_c$ does not vary upon delamination (see Supporting Information for a full comparison of the hysteresis cycles prior to and after delamination). As shown in earlier studies, the magnetoelastic contribution vanishes for this specific composition,[27] suggesting that magnetoelastic effects—that is, a modification of the strain state—is responsible for the observed coercivity changes.

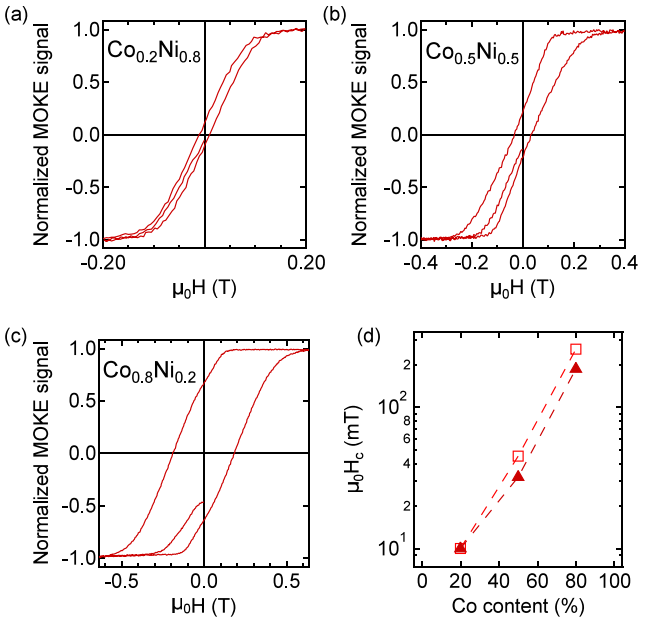

Figure 4. (a-c) Magneto-optical Kerr effect measurements of Co_xNi_{1-x}-$SrTiO_3$ VAN membranes at room temperature, with the magnetic field $\mu_0 H$ applied out-of-plane, parallel to the axis of the nanopillars. (d) Coercive field as a function of the composition x of Co_xNi_{1-x} nanopillars. Squares: values before delamination, triangles: values after delamination.

To quantify the modification of the strain state of the membranes, i.e., the dilation of the matrix and the nanowires before and after delamination, we conducted extensive X-ray diffraction measurements. In what follows, the lattice parameter along the growth axis (parallel to the axis of the nanowires) will be labeled c while a denotes the in-plane lattice parameters. Figure 5 gives a summary of our X-ray diffraction measurements performed on the CoNi-STO membranes (see Supporting Information for a full description of the out-of-plane and in-plane XRD scans). Figures 5a-b show the 002 and

https://doi.org/10.1021/acsanm.6c00973
ACS Appl. Nano Mater. 2026, 9, 9206−9212

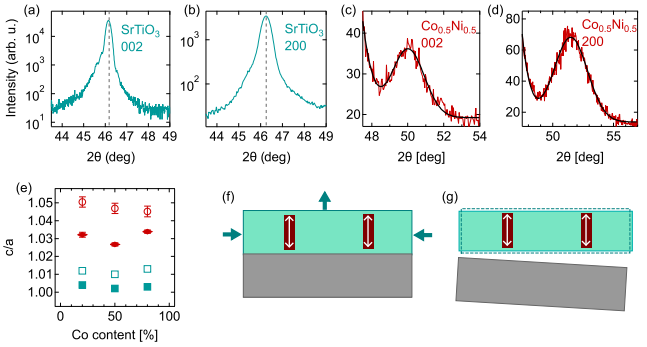

Figure 5. X-ray diffraction measurements before and after delamination and transfer of $Co_{0.5}Ni_{0.5}$-$SrTiO_3$ VAN on Si_3N_4 membranes. Data were collected on a laboratory 5-circle diffractometer (Rigaku SmartLab) with Cu K_α radiation (wavelength of 1.54056 Å). (a-b) $SrTiO_3$ matrix: out-of-plane 002 and in-plane 200 Bragg reflections after delamination. (c-d) $Co_{0.5}Ni_{0.5}$ nanopillars: out-of-plane 002 and in-plane 200 Bragg reflections after delamtination. (e) c/a ratios of the matrix (green) and nanopillars (red) before (open symbols) and after (plain symbols) delamination, as determined by analysis of the XRD measurements. (f-g) Schematic illustrations of the VAN strain state before (f) and after (g) delamination.

200 Bragg reflections of the $SrTiO_3$ matrix while Figures 5c-d show the corresponding 002 and 200 Bragg reflections of the metallic alloy ($Co_{0.5}Ni_{0.5}$). These measurements were performed for the three compositions studied here, which allowed us to extract the c/a ratio before and after lift-off (Figure 5e). The STO matrix is slightly tetragonal with c/a = 1.010 before delamination. This is due to pseudomorphic growth with locking of the in-plane lattice parameter to that of the substrate and vacancy formation during growth.[28,29] Such effects, together with the presence of Ba impurities lead to the out-of-plane lattice expansion. In contrast, the metallic nanopillars exhibit a pronounced tetragonality with $c/a \sim$ 1.04−1.05. Note that while larger tetragonal distortions have been achieved in planar thin films, these are usually only attainable in a few monolayer regime.[30] The unique advantage of the present composite system is that the vertical dilation can be sustained over large distances along the thin film thickness.

How does the strain in the nanocomposites evolve after delamination? Upon removal of the substrate, one would expect the elastic energy stored in the VAN layer to be released, possibly resulting in a largely distinct strain state. In the present case, we do observe a relaxation of the matrix. After lift-off, the tetragonality is almost completely lost, i.e., we obtain an essentially cubic STO lattice. Indeed, the in-plane lattice parameter of the matrix is locked to the one of substrate−a constraint that is lifted upon delamination. In contrast, the tetragonality of the metallic alloy is largely preserved with $c/a \sim 1.03$, irrespective of the concentration. The drop in c/a of the nanowires thus follows the loss of tetragonality of the matrix, as illustrated in Figures 5 f,g. Furthermore, while the c parameter shrinks in the Co_xNi_{1-x} alloy upon delamination ($\Delta c < 0$), the a parameter increases ($\Delta a > 0$). $|\Delta a/\Delta c|$ is in the 0.22 − 0.36 range, consistent with the Poisson ratio $\nu = 0.31$. This strongly supports the fact that the strain in the nanowires is dominated by the vertical heterointerface[13] and that its variation upon delamination is elastic and dictated by the relaxation of the matrix. The large remanent out-of-plane dilation of the metallic Co_xNi_{1-x} nanostructures is one of the main findings of the present study. It demonstrates that unusual strain states can be preserved in a VAN freed from the substrate used for epitaxial growth. In contrast to planar systems, where the substrate removal is accompanied by a loss of the constraints, the delaminated nanocomposites thus remain appealing systems for strain-engineering of physical properties. In the present case, the axial strain within the ferromagnetic nanopillar is a powerful lever to tune the magnetic anisotropy, as demonstrated previously.[22]

In conclusion, we demonstrate the fabrication of free-standing metal−oxide nanocomposite membranes composed of vertically aligned, matrix-embedded nanowires using sacrificial $SrVO_3$ layers and ex-situ transfer steps. The delaminated structures preserve both the metallic character of the embedded nanowires and their unusual strain state, including a significant remanent out-of-plane dilation. These results show that strain-engineered magnetic functionality in vertically aligned nanocomposites can be maintained after full substrate removal. Importantly, the transfer process is not limited to a specific platform but enables integration of the membranes onto arbitrary materials. Our approach thus provides a general route toward substrate-independent implementation of oxide-based nanocomposites, which is particularly relevant for the design of unconventional spintronic architectures, strain-tunable magnetic memory concepts, and magnetoelastic sensing platforms.

■ ASSOCIATED CONTENT

Supporting Information

The Supporting Information is available free of charge at https://pubs.acs.org/doi/10.1021/acsanm.6c00973.

Co_xNi_{1-x}-$SrTiO_3$ VAN growth, delamination and transfer, transmission electron microscopy, XRMS measurements: q-space mapping and Co $L_{2,3}$ edge data, hysteresis loops $M(H)$ before and after delamination, in-plane and out-of-plane XRD scans, peak fitting procedures (PDF)

■ AUTHOR INFORMATION

Corresponding Author

Franck Vidal − *Sorbonne Université, CNRS, Institut des NanoSciences de Paris, INSP, 75005 Paris, France;* orcid.org/0000-0001-7107-9340; Email: franck.vidal@insp.jussieu.fr

Authors

Carlos Alfonso Rodríguez Cortéz − *Sorbonne Université, CNRS, Institut des NanoSciences de Paris, INSP, 75005 Paris, France;* orcid.org/0009-0002-0351-1685

Moussa Mebarki − *Groupe d'Etude de la Matière Condensée (GEMaC), Université de Versailles Saint-Quentin-en-Yvelines, CNRS-UMR8635, Université Paris-Saclay, 78035 Versailles, France*

Bruno Berini − *Groupe d'Etude de la Matière Condensée (GEMaC), Université de Versailles Saint-Quentin-en-Yvelines, CNRS-UMR8635, Université Paris-Saclay, 78035 Versailles, France;* orcid.org/0000-0002-9063-5194

Dominique Demaille − *Sorbonne Université, CNRS, Institut des NanoSciences de Paris, INSP, 75005 Paris, France*

Vincent Polewczyk − *Groupe d'Etude de la Matière Condensée (GEMaC), Université de Versailles Saint-Quentin-*

https://doi.org/10.1021/acsanm.6c00973
ACS Appl. Nano Mater. 2026, 9, 9206−9212

en-Yvelines, CNRS-UMR8635, Université Paris-Saclay, 78035 Versailles, France

Yunlin Jacques Zheng − *Sorbonne Université, CNRS, Institut des NanoSciences de Paris, INSP, 75005 Paris, France*

Pal Bhuyan − *Sorbonne Université, CNRS, Institut des NanoSciences de Paris, INSP, 75005 Paris, France*

Boris Vodungbo − *Sorbonne Université, CNRS, Laboratoire de Chimie Physique Matière et Rayonnement, LCPMR, 75005 Paris, France*

Emmanuelle Jal − *Sorbonne Université, CNRS, Laboratoire de Chimie Physique Matière et Rayonnement, LCPMR, 75005 Paris, France*

Horia Popescu − *Synchrotron SOLEIL, L'Orme des Merisiers, 91190 Saint-Aubin, France*

Nicolas Jaouen − *Synchrotron SOLEIL, L'Orme des Merisiers, 91190 Saint-Aubin, France;* orcid.org/0000-0003-1781-7669

Yves Dumont − *Groupe d'Etude de la Matière Condensée (GEMaC), Université de Versailles Saint-Quentin-en-Yvelines, CNRS-UMR8635, Université Paris-Saclay, 78035 Versailles, France;* orcid.org/0000-0002-0739-428X

Marcel Hennes − *Sorbonne Université, CNRS, Institut des NanoSciences de Paris, INSP, 75005 Paris, France;* orcid.org/0000-0003-3405-9601

Complete contact information is available at: https://pubs.acs.org/10.1021/acsanm.6c00973

Notes

The authors declare no competing financial interest.

■ ACKNOWLEDGMENTS

The authors acknowledge SOLEIL synchrotron for granting beam time (Proposal No. 20241560). We are grateful to the SOLEIL staff for smoothly running the facility. Part of this work is supported by Agence Nationale de la Recherche (ANR-HYPNOSE, project n°21-CE09-0042, ANR-FLEXO, project n°21-CE09-0046 and ANR-SPINMAT, project n°22-EXSP-0007). The authors gratefully thank N. Menguy and J.-M. Guigner, IMPMC, Sorbonne Université-CNRS, for access to the TEM facilities.

■ REFERENCES

(1) Zhang, Y.; Ma, C.; Lu, X.; Liu, M. Recent progress on flexible inorganic single-crystalline functional oxide films for advanced electronics. *Mater. Horiz.* **2019**, *6*, 911.

(2) Mandal, R.; Yun, S.; Wurster, K.; Dollekamp, E.; Shondo, J. N.; Pryds, N. Recent Advancement in Ferroic Freestanding Oxide Nanomembranes. *Nano Lett.* **2025**, *25*, 5541−5549.

(3) Ji, D.; Cai, S.; Paudel, T. R.; Sun, H.; Zhang, C.; Han, L.; Wei, Y.; Zang, Y.; Gu, M.; Zhang, Y.; Gao, W.; Huyan, H.; Guo, W.; Wu, D.; Gu, Z.; Tsymbal, E. Y.; Wang, P.; Nie, Y.; Pan, X. Freestanding crystalline oxide perovskites down to the monolayer limit. *Nature* **2019**, *570*, 87−90.

(4) Lu, D.; Baek, D. J.; Hong, S. S.; Kourkoutis, L. F.; Hikita, Y.; Hwang, H. Y. Synthesis of freestanding single-crystal perovskite films and heterostructures by etching of sacrificial water-soluble layers. *Nat. Mater.* **2016**, *15*, 1255−1260.

(5) Bourlier, Y.; Bérini, B.; Frégnaux, M.; Fouchet, A.; Aureau, D.; Dumont, Y. Transfer of Epitaxial $SrTiO_3$ Nanothick Layers Using Water-Soluble Sacrificial Perovskite Oxides. *ACS Appl. Mater. Interfaces* **2020**, *12*, 8466−8474.

(6) Takahashi, R.; Lippmaa, M. Sacrificial water-soluble BaO layer for fabricating free-standing piezoelectric membranes. *ACS Appl. Mater. Interfaces* **2020**, *12*, 25042−25049.

(7) Ganguly, S.; Pesquera, D.; Garcia, M.; Saeed, U.; Mirzamohammadi, N.; Santiso, J.; Padilla, J.; Roque, J. M. C.; Laulhé, C.; Berenguer, F.; Villanueva, L. G.; Catalan, G. Photostrictive Actuators Based on Freestanding Ferroelectric Membranes. *Adv. Mater.* **2024**, *36*, 2310198.

(8) Huang, J. K.; Wan, Y.; Shi, J.; Zhang, J.; Wang, Z.; Wang, W.; Yang, N.; Liu, Y.; Lin, C. H.; Guan, X.; Hu, L.; Yang, Z. L.; Huang, B. C.; Chiu, Y. P.; Yang, J.; Tung, V.; Wang, D.; Kalantar-Zadeh, K.; Wu, T.; Zu, X.; Qiao, L.; Li, L. J.; Li, S. High-κ perovskite membranes as insulators for two-dimensional transistors. *Nature* **2022**, *605*, 262−267.

(9) Su, Y.; Zong, A.; Kogar, A.; Lu, D.; Hong, S. S.; Freelon, B.; Rohwer, T.; Wang, B. Y.; Hwang, H. Y.; Gedik, N. Delamination-Assisted Ultrafast Wrinkle Formation in a Freestanding Film. *Nano Lett.* **2023**, *23*, 10772−10778.

(10) Degezelle, A.; Burcea, R.; Gemeiner, P.; Vallet, M.; Dkhil, B.; Fusil, S.; Garcia, V.; Matzen, S.; Lecoeur, P.; Maroutian, T. Strain-Induced Polarization Rotation in Freestanding Ferroelectric Oxide Membranes. *Adv. Electron. Mater.* **2025**, *11*, No. e00266.

(11) Sheeraz, M.; Jung, M.-H.; Kim, Y. K.; Lee, N.-J.; Jeong, S.; Choi, J. S.; Jo, Y. J.; Cho, S.; Kim, I. W.; Kim, Y.-M.; Kim, S.; Ahn, C. W.; Yang, S. M.; Jeong, H. Y.; Kim, T. H. Freestanding Oxide Membranes for Epitaxial Ferroelectric Heterojunctions. *ACS Nano* **2023**, *17*, 13510−13521.

(12) Zhang, W.; Chen, A.; Bi, Z.; Jia, Q.; MacManus-Driscoll, J. L.; Wang, H. Interfacial Coupling in Heteroepitaxial Vertically Aligned Nanocomposite Thin Films: From Lateral to Vertical Control. *Curr. Opin. Solid State Mater. Sci.* **2014**, *18*, 6−18.

(13) Chen, A.; Su, Q.; Han, H.; Enriquez, E.; Jia, Q. Metal Oxide Nanocomposites: A Perspective from Strain, Defect, and Interface. *Adv. Mater.* **2019**, *31*, 1803241.

(14) Chen, A.; Bi, Z.; Jia, Q.; MacManus-Driscoll, J. L.; Wang, H. Microstructure, vertical strain control and tunable functionalities in self-assembled, vertically aligned nanocomposite thin films. *Acta Mater.* **2013**, *61*, 2783−2792.

(15) Liu, H.-J.; Chen, L.-Y.; He, Q.; Liang, C.-W.; Chen, Y.-Z.; Chien, Y.-S.; Hsieh, Y.-H.; Lin, S.-J.; Arenholz, E.; Luo, C.-W.; Chueh, Y.-L.; Chen, Y.-C.; Chu, Y.-H. Epitaxial photostriction−magnetostriction coupled self-assembled nanostructures. *ACS Nano* **2012**, *6*, 6952−6959.

(16) Chen, A.; Jia, Q. A pathway to desired functionalities in vertically aligned nanocomposites and related architectures. *MRS Bull.* **2021**, *46* (2021), 115.

(17) Hennes, M.; Demaille, D.; Patriarche, G.; Tran, T.; Zheng, Y.; Vidal, F. Strain, magnetic anisotropy, and composition modulation in hybrid metal-oxide vertically assembled nanocomposites. *MRS Bull.* **2021**, *46* (2021), 136.

(18) Huang, J.; Tsai, B. K.; Choudhury, A.; Shen, J.; Mihalko, C. A.; Zhou, S.; Liu, C.; Wang, H. Freestanding TiN-Au Vertically Aligned Nanocomposite Thin Films for Flexible Plasmonic Hybrid Metasurfaces. *Adv. Mater. Interfaces* **2025**, *12*, No. e00613.

(19) Tsai, B. K.; Huang, J.; Yu, Y.-C.; Lee, M. H.; Stegman, B. T.; Flores, E. J.; Tong, P. Z.; Xu, K.; Zhou, S.; Shen, J.; Song, J.; Zhang, Y.; Stanciu, L.; Wu, W.; Zhang, X.; Wang, H. Freestanding $BaTiO_3$-Au Vertically Aligned Nanocomposite toward Flexible Multi-Sensing Platform. *Adv. Funct. Mater.* **2025**, *35*, 2418004.

(20) Bonilla, F. J.; Novikova, A.; Vidal, F.; Zheng, Y. L.; Fonda, E.; Demaille, D.; Schuler, V.; Coati, A.; Vlad, A.; Garreau, Y.; Sauvage Simkin, M.; Dumont, Y.; Hidki, S.; Etgens, V. Combinatorial Growth and Anisotropy Control of Self-Assembled Epitaxial Ultrathin Alloy Nanowires. *ACS Nano* **2013**, *7*, 4022−4029.

(21) Weng, X.; Hennes, M.; Coati, A.; Vlad, A.; Garreau, Y.; Sauvage-Simkin, M.; Fonda, E.; Patriarche, G.; Demaille, D.; Vidal, F.; Zheng, Y. Ultrathin Ni nanowires embedded in $SrTiO_3$: Vertical epitaxy, strain relaxation mechanisms, and solid-state amorphization. *Phys. Rev. Mater.* **2018**, *2*, 106003.

(22) Weng, X.; Hennes, M.; Juhin, A.; Sainctavit, Ph.; Gobaut, B.; Otero, E.; Choueikani, F.; Ohresser, P.; Tran, T.; Hrabovsky, D.; Demaille, D.; Zheng, Y.; Vidal, F. Strain-engineering of magnetic

anisotropy in Co_xNi_{1-x}-$SrTiO_3$/$SrTiO_3$(001) vertically assembled nanocomposites. *Phys. Rev. Mater.* **2022**, *6*, 046001.
(23) Huang, J.; Li, L.; Hu, Z.; Tsai, B. K.; Huang, J.; Shen, J.; Zhang, Y.; Barnard, J. P.; Song, J.; Wang, H. Ultrathin Ternary FeCoNi Alloy Nanoarrays in $BaTiO_3$ Matrix for Room-Temperature Multiferroic and Hyperbolic Metamaterial. *Nano Lett.* **2024**, *24*, 10081−10089.
(24) Fouchet, A.; Allain, M.; Bérini, B.; Popova, E.; Janolin, P.-E.; Guiblin, N.; Chikoidze, E.; Scola, J.; Hrabovsky, D.; Dumont, Y.; et al. Study of the electronic phase transition with low dimensionality in $SrVO_3$ thin films. *Materials Science and Engineering: B* **2016**, *212*, 7−13.
(25) Popescu, H.; Perron, J.; Pilette, B.; Vacheresse, R.; Pinty, V.; Gaudemer, R.; Sacchi, M.; Delaunay, R.; Fortuna, F.; Medjoubi, K.; Desjardins, K.; Luning, J.; Jaouen, N. COMET: a new end-station at SOLEIL for coherent magnetic scattering in transmission. *J. Synchrotron Radiat.* **2019**, *26*, 280.
(26) Rackham, J.; Pratt, B.; Griner, D.; Smith, D.; Cai, Y.; Harrison, R. G.; Reid, A.; Kortright, J.; Transtrum, M. K.; Chesnel, K. Field-dependent nanospin ordering in monolayers of Fe_3O_4 nanoparticles throughout the superparamagnetic blocking transition. *Phys. Rev. B* **2023**, *108*, 104415.
(27) Kadowaki, S.; Takahashi, M. Magnetostriction Constants of Nickel-Cobalt Alloys. *J. Phys. Soc. Jpn.* **1981**, *50*, 1154−1161.
(28) Ohnishi, T.; Shibuya, K.; Yamamoto, T.; Lippmaa, M. Defects and transport in complex oxide thin films. *J. Appl. Phys.* **2008**, *103*, 103703.
(29) Keeble, D. J.; Wicklein, S.; Dittmann, R.; Ravelli, L.; Mackie, R. A.; Egger, W. Identification of A- and B-Site Cation Vacancy Defects in Perovskite Oxide Thin Films. *Phys. Rev. Lett.* **2010**, *105*, 226102.
(30) Winkelmann, A.; Przybylski, M.; Luo, F.; Shi, Y.; Barthel, J. Perpendicular Magnetic Anisotropy Induced by Tetragonal Distortion of FeCo Alloy Films Grown on Pd(001). *Phys. Rev. Lett.* **2006**, *96*, 257205.

https://doi.org/10.1021/acsanm.6c00973
ACS Appl. Nano Mater. 2026, 9, 9206−9212